SCIENCE CHINA
Technological Sciences

•Article•

May 2020 Vol.63 No.5: 755–767
https://doi.org/10.1007/s11431-019-1449-4

Fracture characterization and permeability prediction by pore scale variables extracted from X-ray CT images of porous geomaterials

ZHAO Zhi[1], ZHOU Xiao-Ping[1*] & QIAN Qi-Hu[2]

[1] *School of Civil Engineering, Chongqing University, Chongqing 400045, China;*
[2] *State Key Laboratory of Disaster Prevention and Mitigation of Explosion and Impact, PLA University of Science and Technology, Nanjing 210014, China*

Received June 22, 2019; accepted September 17, 2019; published online January 14, 2020

Pore scale variables (e.g., porosity, grain size) are important indexes to predict the hydraulic properties of porous geomaterials. X-ray images from ten types of intact sandstones and another type of sandstone samples subjected to triaxial compression are used to investigate the permeability and fracture characteristics. A novel double threshold segmentation algorithm is proposed to segment cracks, pores and grains, and pore scale variables are defined and extracted from these X-ray CT images to study the geometric characteristics of microstructures of porous geomaterials. Moreover, novel relations among these pore scale variables for permeability prediction are established, and the evolution process of cracks is investigated. The results indicate that the pore-scale permeability is prominently improved by cracks. In addition, excellent agreements are found between the measured and the estimated pore scale variables and permeability. The established correlations can be employed to effectively identify the hydraulic properties of porous geomaterials.

sandstones, X-ray CT images, pore scale variables, permeability prediction, cracks characterization

Citation: Zhao Z, Zhou X P, Qian Q H. Fracture characterization and permeability prediction by pore scale variables extracted from X-ray CT images of porous geomaterials. Sci China Tech Sci, 2020, 63: 755–767, https://doi.org/10.1007/s11431-019-1449-4

1 Introduction

The permeability is one of the most important factors that involves in the oil-gas resources exploration [1,2], storage and isolation of carbon dioxide [3,4] and safety problem of engineering practices [5–7]. In recent decades, various methods are applied to investigate the permeability. Darcy law as the most basic permeability estimation method is widely used. However, it may lead to inevitable errors caused by viscous fingering and high injection rates in the tests [8,9]. Moreover, the core analysis of geomaterials is extensively applied, in which the permeability can be directly obtained [10,11]. However, it is limited to the data absence of entire intervals and vertical plugs collection. Considering these problems, artificial intelligence models based on computer intelligence are introduced to estimate the permeability such as neural network [12], fuzzy logic [13] and genetic algorithm [14]. Unfortunately, despite of their great contributions to parameter prediction and wide application, most of these models are time consuming and trapped in the local minima problem, which is limited to the datasets of samples, learning algorithms and network topologies of the computing models.

In addition, various numerical models are constructed to evaluate the permeability by pore scale variables (e.g., porosity, grain size) [15–18], and the permeability is also extremely affected by crack types and crack propagation mechanism in geomaterials [19–22]. In fact, pore scale

*Corresponding author (xiao_ping_zhou@126.com)

variables in geomaterials are extremely affected by geological process during rock formation [23–25]. Understanding these variables is helpful to evaluate the hydraulic and mechanical properties of porous geomaterials [26,27]. Jobmann and Billaux [28] proposed an interesting correlation to predict the permeability by porosity and pore radius in opalinus clay. Zheng et al. [29] presented a permeability relation by porosity and effective stress of sedimentary rock based on Two-parts Hooke's model (TPHM). Ingraham et al. [30] discussed the permeability evolution based on the constant mean stress and shear stress in high porosity sandstone reservoirs. Alyafei and Blunt [31] provided novel procedures to obtain the imbibition constant to calculate imbibition relative permeability and capillary pressure from mass imbibition dataset. To date, with the development of X-ray CT imaging technologies, we can get more insights to the pore and grain structures of geomaterails [32,33]. Latief et al. [34] quantitatively described the 3D pore geometry reconstructed by 3D pigeon hole, and defined the porosity, pore radius and specific surface. Du et al. [35] proposed a novel volumetric coupled heat transfer model of solar receiver at pore-scale to study the fluid flow and heat transfer in volumetric solar based on the X-ray computed tomography technique. Sun and Wong [36] gained a permeability relation of sandstone using hybrid lattice Boltzmann simulation on X-ray CT images. Zhao and Zhou [37] proposed an integrated method to reconstruct the 3D pore-scale models based on 2D X-ray CT images, and to predict the permeability. Yang et al. [38] studied the effects of varying pore scale variables, non-even distribution of hydrates and fluid flow directions on the absolute and relative permeability based on the X-ray CT imaging techniques.

However, although the previous studies have offered fine relations for permeability estimation, these permeability correlations are concluded by only either porosity or grain size with no consideration of their comprehensive effect on permeability. Moreover, with the improvement of X-ray nondestructive testing, there should be a simpler correlation for the permeability estimation based on pore scale variables. In addition, the effect of cracks on the pore-scale permeability is not yet well understood. Therefore, the main purposes are to evaluate the pore scale variables and to establish effective relation of permeability with simple implementations. In this paper, X-ray CT imaging techniques are applied to capture the microstructure information of sandstone samples. The double threshold segmentation method is proposed to accurately segment the cracks, pores and grains. Moreover, the pore scale variables are defined by the proposed double threshold segmentation algorithm. Furthermore, the novel correlations for permeability estimation among these pore variables are established. In addition, the crack effect on the pore-scale permeability is studied. Compared with the previous works, the main advantages of this works are (1) the accurate segmentation of cracks-pores structures with similar gray levels by the proposed double threshold segmentation algorithm; (2) quantitative study of the fracturing behaviors by the defined pore-scale variables; (3) novel specific surface relation of porosity and grain size; (4) the simple implementation to rapidly calculate the pore-scale permeability by the proposed novel relation based on pore scale variables.

This paper is organized as follows. Sect. 2 describes the samples and methods for pore scale variables extraction, and establishes the novel correlations and validation models of specific surfaces for permeability estimation. Sect. 3 shows the fracture characteristics and hydraulic properties evaluated by the established correlations, and simple summaries and conclusions are drawn in Sect. 4.

2 Specimen description and methodologies

2.1 Specimen description

In this study, 11 types of sandstone specimens [39] labeled by S1–S11 are used to investigate the fracturing and hydraulic properties by extracting the pore scale variables from X-ray CT images. The helium porosity and air average permeability are measured by the AP608 automated Permeameter-Porosimeter. Moreover, to investigate the fracture characteristics, sandstone S11 is scanned before and after the triaxial compression tests. The detailed basic parameters of these types of sandstone specimens are listed in Table 1.

2.2 Methodology

Determining the hydraulic and fracturing behaviors of porous geomaterials is a challengeable task due to its complex pore structures. The main issue to obtain the values of pore scale variables is to extract reliable and available information from X-ray CT images using the image processing algorithm. The recognition of pores and cracks is crucial to investigate the fracturing behaviors and to study the permeability of geomaterials. In this paper, a double threshold segmentation algorithm is proposed to obtain accurate segmentation results of pores and cracks in sandstones. Moreover, the pore scale variables are extracted from the X-ray CT images using this proposed algorithm. Once the pore scale variables are determined, the relations among these variables can be established. Thus, the permeability and fracturing behaviors can be studied.

2.2.1 Segmentation of pores and cracks

Pores and cracks are the primary structural components in geomaterials. Therefore, the segmentation of pores and cracks are crucial to identify the fracture behaviors and hydraulic properties. Common segmentation algorithms are limited to the gray level differences between pores and

Table 1 Parameters of selected sandstone specimens[a)]

Types	S1	S2	S3	S4	S5	S6	S7	S8	S9	S10	S11
Resolution (μm/pixel)	5.35	8.68	4.96	9.1	8.96	4	5.1	4.8	4.89	3.4	8.01
Pixel-scale	300^2	300^2	300^2	300^2	300^2	300^2	300^2	300^2	300^2	300^2	300^2
Slices	300	300	300	300	300	300	300	300	300	300	100
G (kN/m^3)	23.25	23.28	22.97	23.35	22.88	23.12	23.15	22.89	23.11	23.15	22.89
φ	0.188	0.141	0.238	0.152	0.158	0.218	0.238	0.245	0.351	0.223	0.163
κ (mD)	279	332	550	223	251	517	594	767	706	364	172

a) G-unit weight, κ-permeability

cracks, which can not be directly applied to the segmentation of grains, pores and cracks. In these cases, the common segmentation algorithm of pores and grains is replaced by the proposed double threshold segmentation algorithm of cracks, pores and grains. Different from the classical segmentation algorithm, two optimal threshold values are defined to segment cracks, pores and grains. In brief, this proposed approach is depicted as follows.

The relative frequency statistics of gray intensity values in an arbitrary $N\times N$ X-ray CT image are first calculated by

$$Fs=\sum_{i=0}^{N-1}\sum_{j=0}^{N-1}f(x,y),\ f(x,y)\in[0,255], \tag{1}$$

where $f(x,y)$ and Fs are the gray intensity and the relative frequency statistics in the unique gray intensity varying from 0 to 255, respectively.

An arbitrary crack segmentation threshold value T_1 marches along Fs, which is divided into two classes $Fs_1[\min(f)\rightarrow T_1]$ and $Fs_2[T_1\rightarrow\max(f)]$. The variances of these two classes are separately computed by

$$\chi_1^{C}(T_1)=\frac{\sum_{i=1}^{\Im(Fs_1)}\left[Fs_1(i)-\sum_{i=1}^{\Im(Fs_1)}Fs_1(i)/\Im(Fs_1)\right]^2}{\Im(Fs_1)-1}, \tag{2}$$

$$\chi_2^{C}(T_1)=\frac{\sum_{i=1}^{\Im(Fs_2)}\left[Fs_2(i)-\sum_{i=1}^{\Im(Fs_2)}Fs_2(i)/\Im(Fs_2)\right]^2}{\Im(Fs_2)-1}, \tag{3}$$

where $\Im$ is the count function of f, χ_1^{C} and χ_2^{C} are respectively the variances for crack segmentation between Fs_1 and Fs_2, and $Fs_1(i)$ and $Fs_2(i)$ are respectively the gray intensity of the ith pixel.

Thus, the optimal threshold to segment the crack can be determined by

$$T_C=\wp\left[\max\left(\left|\chi_1^{C}(T_1)-\chi_2^{C}(T_1)\right|\right)\right],\ T_1\in[\min(f),\max(f)], \tag{4}$$

where $\wp$ denotes the searching function of the maximum of absolute difference between χ_1^{C} and χ_2^{C}.

Once the crack segmentation threshold value is determined, cracks can be segmented and excluded in the pore segmentation procedure. During the pore segmentation, the gray intensity values in crack regions are replaced by Nan, which are not utilized in the searching procedure of the optimal pore segmentation threshold.

Similar to the crack segmentation procedure, an arbitrary threshold value T_2 is selected to scan the rebuilt relative frequency statistics Fs excluding the crack region. Obviously, the renewed frequency statistics Fs is divided into two parts $Fs_1\varnothing\mathrm{Nan}[\min(f)\rightarrow T_2]$ and $Fs_2\varnothing\mathrm{Nan}[T_2\rightarrow\max(f)]$ in the same way as the crack segmentation procedure. Thus, the variances of the two parts can be computed by

$$\chi_1^{P}(T_2)=\frac{\sum_{i=1}^{\Im(Fs_1\varnothing\mathrm{Nan})}\left[Fs_1\varnothing\mathrm{Nan}(i)-\sum_{i=1}^{\Im(Fs_1\varnothing\mathrm{Nan})}Fs_1\varnothing\mathrm{Nan}(i)/\Im(Fs_1\varnothing\mathrm{Nan})\right]^2}{\Im(Fs_1\varnothing\mathrm{Nan})-1}, \tag{5}$$

$$\chi_2^{P}(T_2)=\frac{\sum_{i=1}^{\Im(Fs_2\varnothing\mathrm{Nan})}\left[Fs_2\varnothing\mathrm{Nan}(i)-\sum_{i=1}^{\Im(Fs_2\varnothing\mathrm{Nan})}Fs_2\varnothing\mathrm{Nan}(i)/\Im(Fs_2\varnothing\mathrm{Nan})\right]^2}{\Im(Fs_2\varnothing\mathrm{Nan})-1}, \tag{6}$$

where $Fs_1\varnothing\mathrm{Nan}$ and $Fs_2\varnothing\mathrm{Nan}$ respectively denote the renewed gray intensity dataset without crack region in the left and right classes, $Fs_1\varnothing\mathrm{Nan}(i)$ and $Fs_2\varnothing\mathrm{Nan}(i)$ are respectively the gray intensity in the ith pixel, χ_1^{P} and χ_2^{P} are respectively the variances for pore segmentation between $Fs_1\varnothing\mathrm{Nan}$ and $Fs_2\varnothing\mathrm{Nan}$.

Then, the optimal pore segmentation can be determined by

$$T_P=\wp\left[\max\left(\left|\chi_1^{P}(T_2)-\chi_2^{P}(T_2)\right|\right)\right],\ T_2\in[\min(f),\max(f)]. \tag{7}$$

2.2.2 *Representation of crack, pores and grains*

Generally, after the optimal crack and pore segmentation threshold values are determined, the cracks, pores and grains can be segmented by

$$f_{\mathrm{b}}=\begin{cases}\mathrm{Nan}, & f\in[0,T_C];\ \text{for cracks},\\ 0, & f\in[T_C,T_p];\ \text{for pores},\\ 1, & f\in[T_P,255];\ \text{for grains},\end{cases} \tag{8}$$

where f_{b} is the binary value of each gray intensity value.

In fact, to represent the segmented X-ray CT image intuitively, the binary values in crack region are also replaced by 0 during the visualization process of the segmented image. Finally, the segmented image is represented as a binary image. Crack and pores are represented by black (0), and grains are represented by white (1).

Usually, the gray intensity values of structural components of sandstones are defined by its density. The lower the density, the blacker the pixel and the lower the gray intensity. Thus, the cracks, pores and grains can be segmented well using the proposed double threshold segmentation algorithm. Figure 1 shows the diagrams to obtain the segmented pores, cracks and grains image. Figure 1(a) shows the pore segmentation of the X-ray CT image from an intact sandstone sample by eqs. (2)–(4) and (8). Figure 1(b) displays the segmentation of crack, pores and grains by eqs. (5)–(8). The segmentation threshold values are 118.9 for pores in the intact samples, 50.6 and 123.6 for crack and pores in damaged samples, respectively. Based on these threshold values, the microscopic crack, pores and grains networks are determined. Figure 2 shows the sketch maps of original images, binary pore-grain images and color images from sandstone specimens S4, S9 and S10, respectively. In the binary images, the pores are black and grains are whites. Moreover, the pores in the color images of samples are represented in different colors to distinguish different pores with different pore size, as shown in Figure 2(c). In addition, the grains can also be represented in different colors in the same way of color pores representation. The color representations of pores and grains are applied to calculate the pore and grain size later.

2.3 Extraction of pore scale variables

While the structural components of the sandstone are obtained using the proposed segmentation algorithm, pore scale variables used to investigate the hydraulic and fracturing behaviors can be extracted from the segmented 2D and 3D images. Damage ratio, porosity and grain ratio are important factors to study the evolution process of cracks. According to the definition of the damage ratio in previous studies [40–42] and the proposed segmentation techniques, the damage ratio, porosity and grain ratio at microscale in this paper are respectively redefined as

$$\begin{cases} \psi = \dfrac{\Im(f_{\to \mathbb{Q}_{\mathrm{Nan}}})}{\Im(f_{\to \mathbb{Q}})}, & f \in Q_{\mathrm{Nan}}, \\ \varphi = \dfrac{\Im(f_{\to \mathbb{Q}_0})}{\Im(f_{\to \mathbb{Q}})}, & f \in Q_0, \\ \phi = \dfrac{\Im(f_{\to \mathbb{Q}1})}{\Im(f_{\to \mathbb{Q}})}, & f \in Q_1, \end{cases} \tag{9}$$

where ψ, φ and ϕ are the damage ratio, porosity and grains ratio, respectively; Q and Q_i(i=Nan, 0, 1) are the total set and subsets of the gray intensity representing different structural components in the X-ray CT image.

Figure 3 shows the sketch maps of 3D pores and grains models of sandstone specimen S8, pores and grains are shown in different colors. Thus, from Figure 3 and eq. (9), the porosity and corresponding grains ratio can be calculated.

Once the damage ratio, porosity and grains ratio are extracted, the fracture and hydraulic properties of the sandstones can be investigated. The permeability as an important factor is applied to investigate the hydraulic properties of geomaterials, which is usually studied using the Nuclear Magnetic Resonance (NMR) method [43], Lattice Boltzmann method [44,45], Kozeny-Carman equation of porous geomaterials [46–48], computational fluid dynamic [49] and Level-set methods [50]. In addition, the Kozeny-Carman equation is widely applied to investigate the permeability of porous geomaterials, and the permeability can be computed by [46–52]

$$\kappa = \frac{\varphi^3}{h(1-\varphi)^2 \xi^2}, \tag{10}$$

where κ, ξ and h are the permeability, specific surface and Kozeny-Carman constant determined by pore shapes, respectively.

Apparently, to obtain the permeability, the values of Kozeny-Carman constant and specific surface should be first determined. In fact, specific surface denotes the ratio of interstitial surface area of grains per unit to total grains volume, which can be computed by [53,54]

$$\xi = \sum A_{\mathrm{grain}} / \sum V_{\mathrm{grain}}, \tag{11}$$

where A_{grain} and V_{grain} respectively denote the surface area and volume of the grains, as shown in Figure 4(b).

Actually, to compute the grain size and the surface area, each color bulk volume in sandstone is computed by the number of pixel with the same color. Then, each color bulk is supposed as the equivalent sphere. Figure 4 schematically illustrates the rules to convert color bulks to spheres, in which each color bulk represents each grain size composed by unit cubic pixel in the pixel matrix. Thus, the grain size can be computed by

$$\lambda_i = 2 \times \sqrt[3]{\frac{3 \times \Im(f \to C_i)}{4\pi}}, \quad i \in [1, \Im(C)], \tag{12}$$

where λ and C are the grain sizes and color bulks of grains, respectively.

Next, once the grain size is determined, the specific surface should be computed by Eq. (11). In fact, for sphere, the specific surface can be modified as

$$\xi_i = \frac{\pi(\lambda_i/2)^2}{\frac{4}{3}\pi(\lambda_i/2)^3} = \frac{6}{\lambda_i}. \tag{13}$$

In addition, it is obvious that pores and grains are two structural components in X-ray CT images. Namely, there

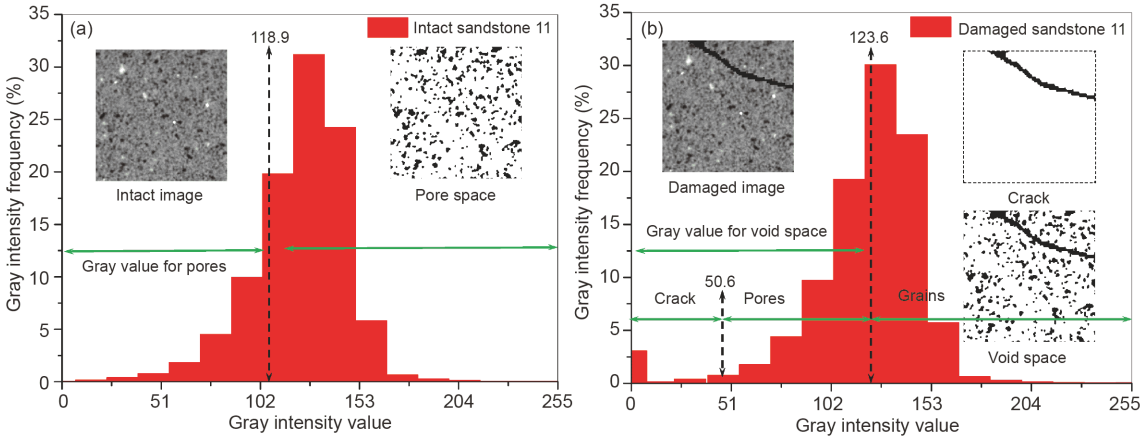

Figure 1 Pore and crack segmentation demonstration using double threshold algorithm.

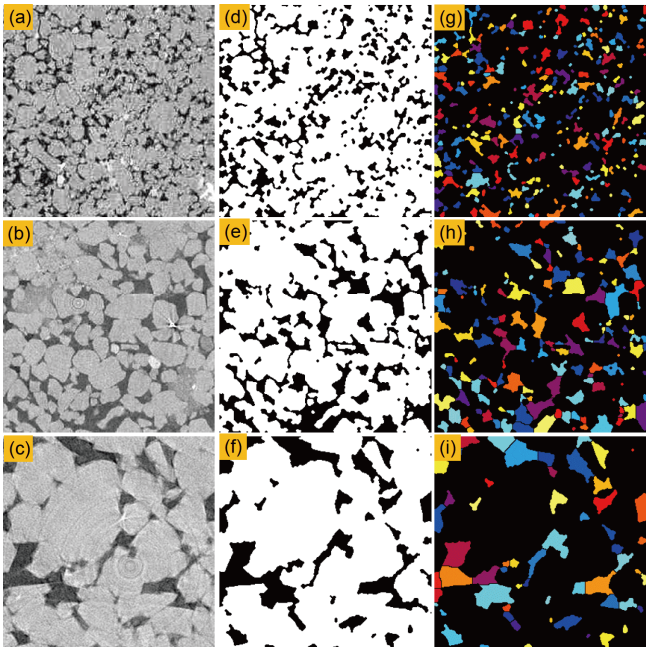

Figure 2 Microstructures of sandstone samples S4, S9 and S10 for (a)–(c) original images; (d)–(f) binary images (pores presented by black and grains presented by white); (g)–(i) color images (pores with sizes presented by different colors and grains presented by black), respectively.

are meaningful correlations between the porosity and specific surface. From the specific surfaces and porosities of 11 fine, medium and coarse pores sandstone specimens, it is found that the specific surface of the grain increases as the porosity decreases. Figure 5 shows the correlation between the porosity and specific surface for fine (S11) medium (S3) and coarse (S8) pore sandstone specimens, respectively. As shown in Figure 5, the general relation between porosity and specific surface can be simply obtained using the Large-scale Unconstrained Non-linear Optimization Algorithm from MATLAB Optimization Toolbox, and is described as

$$\xi = \alpha(1-\varphi), \tag{14}$$

where α is the correlation factor between specific surface and porosity.

From eqs. (13) and (14), it is easy to find the meaningful relations among porosity, grain size and specific surface, which are written as

$$\xi \propto \alpha(1-\varphi), \ \ \xi \propto \frac{\beta}{\bar{\lambda}}, \tag{15}$$

where β is the correlation factor between specific surface and grain size.

To re-establish the relations among specific surface, porosity and grain size, a correlation factor would be applied to fit the relation. The final modified correlation is expressed as

$$\xi = \alpha(1-\varphi) \times \frac{\beta}{\bar{\lambda}} = \gamma \frac{1-\varphi}{\bar{\lambda}}, \tag{16}$$

where γ is the comprehensive correlation factor of α and β.

2.4 Verification for novel specific surface correlation

To validate the accuracy and predictability of the correlation among porosity, grain size and specific surface, a 3D micro pore network prediction (MPNP) model and the 3D real models (Figure 6) of fine, medium and coarse pore sandstone samples are constructed. By integrating the micro structural features of these 11 sandstone samples shown in Figures 4 and 6, the 3D MPNP model is constructed. Figure 7 schematically illustrates the construction procedure of the 3D MPNP model.

The 3D MPNP model is composed by pores and grains in spheres converted by cubic bulks. In this model, porosity is approximately considered to be the same for all fabrics in each grain bulks. Thus, based on this proposed model, eq. (11) can be modified as

$$\xi = \frac{\Im(\mathbb{C})\pi(\bar{\lambda})^2}{\varsigma_b(1-\varphi)(1+\varphi^2+\varphi^3)}, \tag{17}$$

where ζ_b represents the bulk volume of color grains.

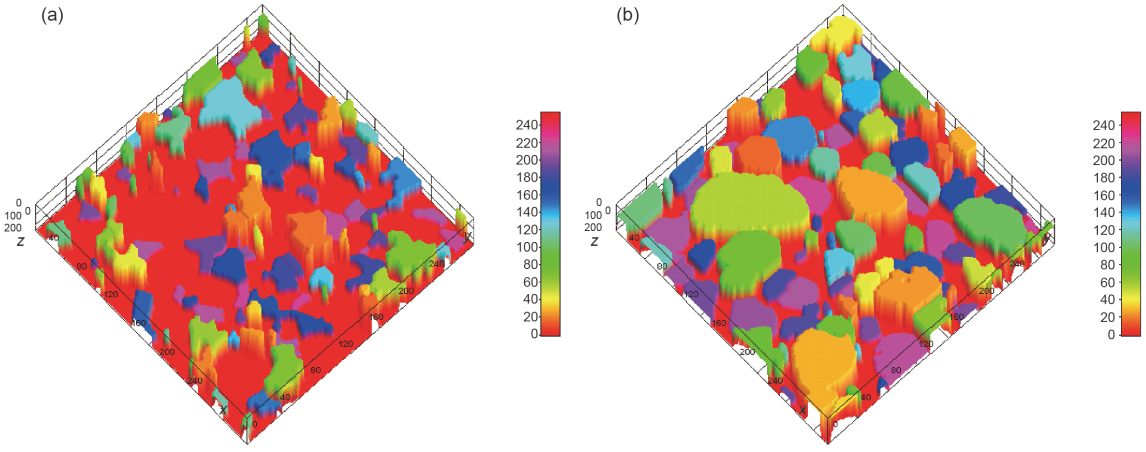

Figure 3 3D Sketch maps of (a) pores with different color bulks and (b) grains with different color bulks from sandstone specimen S8.

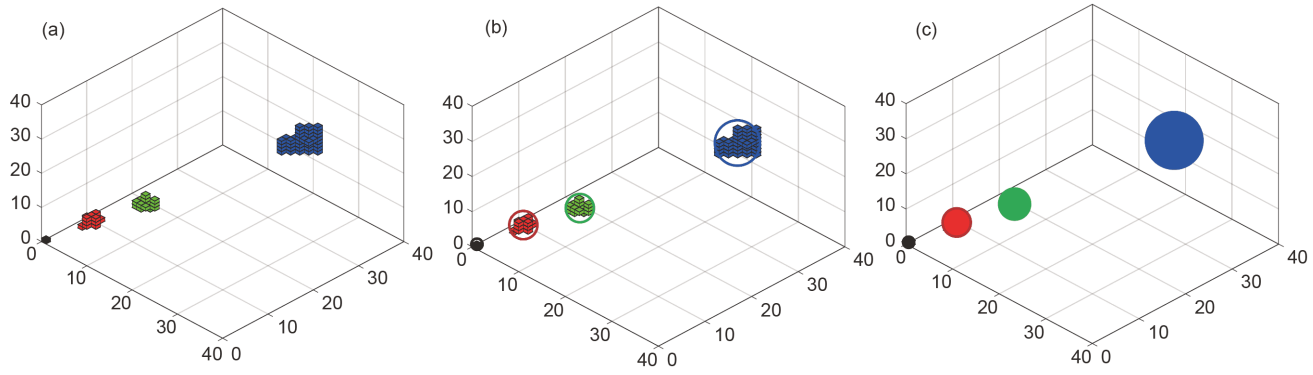

Figure 4 Sketch maps of converting unit cubic pixel grains to spheres.

In fact, the bulk volume of color grains is related to the total volume of spherical color grains by considering a correlation factor λ, and can be computed by

$$\varsigma_b = \lambda \frac{\Im(\mathbb{C})\pi\lambda^3}{6}. \tag{18}$$

Submitting eq.(18) into eq.(17), the relation among porosity, grain size and specific surface can be rewritten as

$$\xi = \frac{6/\lambda}{(1-\varphi)(1+\varphi^2+\varphi^3)\lambda}. \tag{19}$$

In this study, γ=6/λ is assumed to be the comprehensive correlation factor determined by different number of samples with different porosities and grain sizes, which is expressed as

$$\gamma_n = \xi\lambda \sum_{j=0}^{n} (-1)^j \varphi^j, \tag{20}$$

where γ_n denotes the comprehensive correlation factor with different porosities and grain sizes from n samples.

In fact, the porosity varies from 0 to 1, based on Taylor expansion theorem, the general expression of the porosity geometric sequences of sandstone samples can be expressed as

$$\sum_{j=0}^{n} (-1)^j \varphi^j = 1 - \varphi + \varphi^2 - \varphi^3 + \varphi^4 - \cdots = \frac{1}{1-\varphi}. \tag{21}$$

Submitting eq. (21) into eq. (20), it is easy to find that the specific surface can be computed by porosity and grain size in following form

$$\xi = \gamma \frac{1-\varphi}{\lambda}. \tag{22}$$

Apparently, eq. (22) is the same as eq. (16). Thus, we can state that it is accurate and reliable to estimate the specific surface by the correlations derived from porosity and gain size. By replacing the specific surface in eq. (10) by eq. (22), the permeability can be rewritten as

$$\kappa = \frac{\lambda^2 \varphi^3}{\gamma^2 \hbar (1-\varphi)^4}. \tag{23}$$

3 Results and discussion

In this study, X-ray CT datasets are obtained from 11 types of sandstone samples (Figure 1), which contain fine, medium and coarse pore sandstone samples. The former ten types of

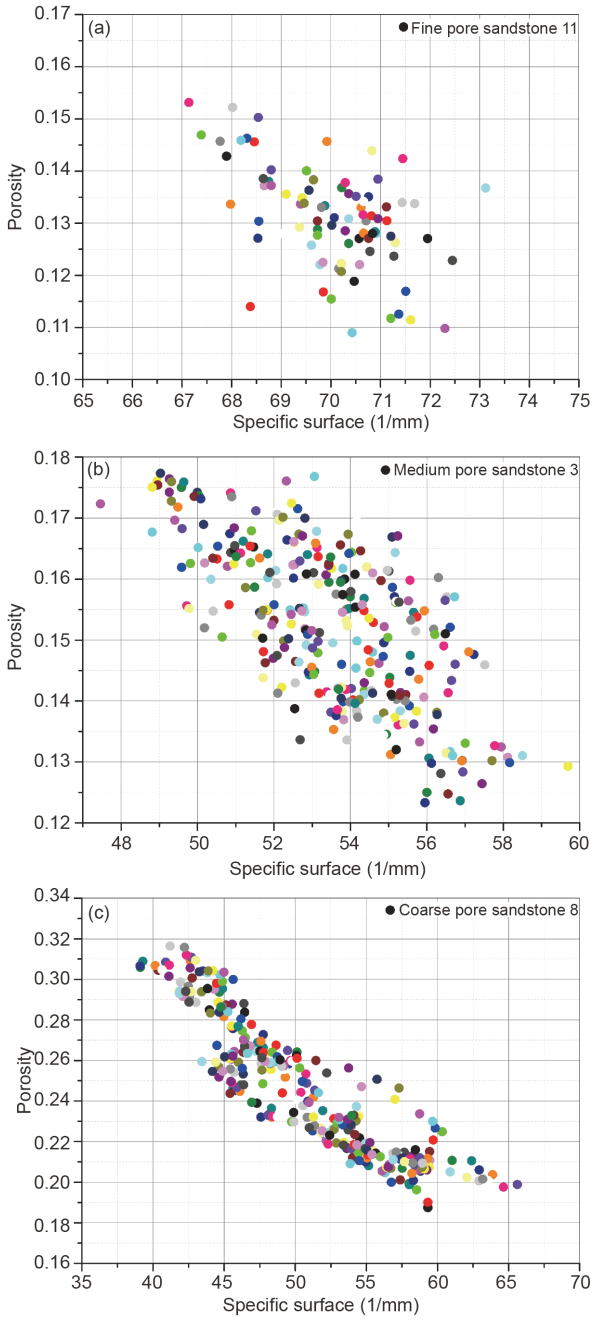

Figure 5 Porosity versus specific surface of (a) S11, (b) S3 and (c) S8 for fine, medium and coarse pore sandstones.

sandstone samples are employed to investigate the relations among the pore scale variables and to predict the permeability. The other type sandstone samples are applied to study the fracturing behaviors of sandstone. The effects of cracks on the sandstone permeability are also analyzed.

3.1 Fracture evolution process

The sandstone samples are failed under triaxial compression with the confining pressure of 20 MPa. Considering the similar failure modes of these sandstone samples, sandstone samples S11 are selected to describe the evolution process of cracks by eqs. (9) and (16). Figure 8 shows the damage ratio and equivalent specific surface of the crack with corresponding crack images at each stage. The evolution process of the crack is classified into 5 phases, as shown in Figure 8(a). In the phase I, the crack grows as the axial stress increases in a nearly linear way. The crack propagates from the top to the bottom of the sample. As the continuous increase of the axial stress, the macroscopic crack propagates stably, as shown in the phase II. With the continuous propagation of the macroscopic crack, it gradually becomes unstable, as shown in the phase III. As the sustaining increase of axial loading, a secondary crack initiates and propagates, and the damage ratio of cracks fluctuates sharply, as shown in the phase IV. In the phase V, the sandstone sample is failed. Figure 8(b) illustrates the change of the specific surface. In the phase I, the crack is initially considered as a color band due to the propagation of the crack, and it can be further divided into more color sub-bands for specific surface. Thus, the average specific surface decreases in a linear way. As the crack propagates in stable way, the number of color sub-bands and their volumes keep almost constant, and the value of specific

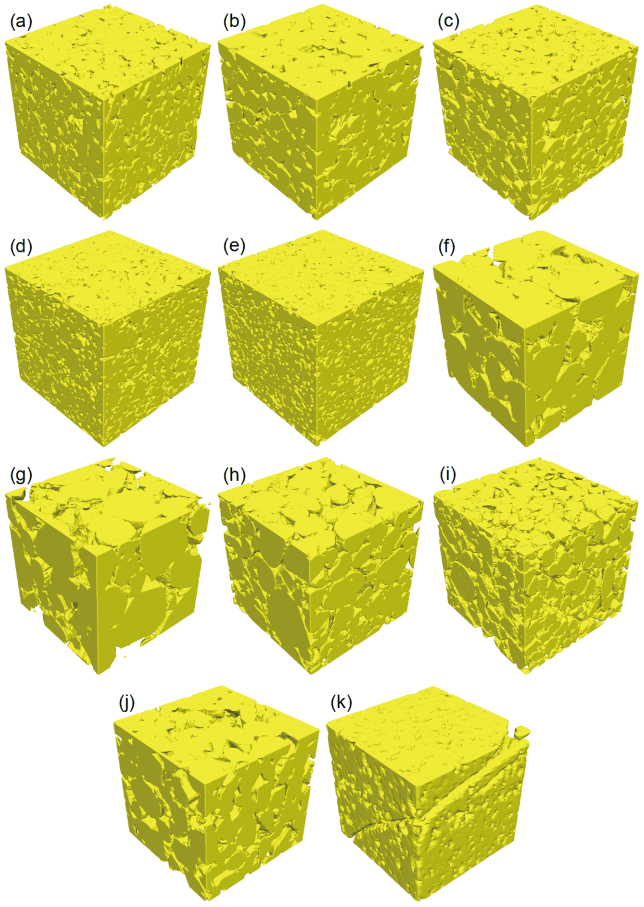

Figure 6 Real 3D pore models of sandstone samples S1–S10 (a)–(j) and fracture model of sandstone sample S11 (k).

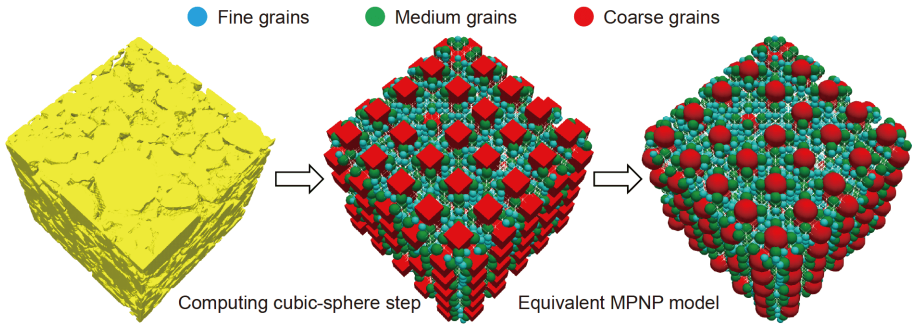

Figure 7 Sketch maps of constructing 3D MPNP model.

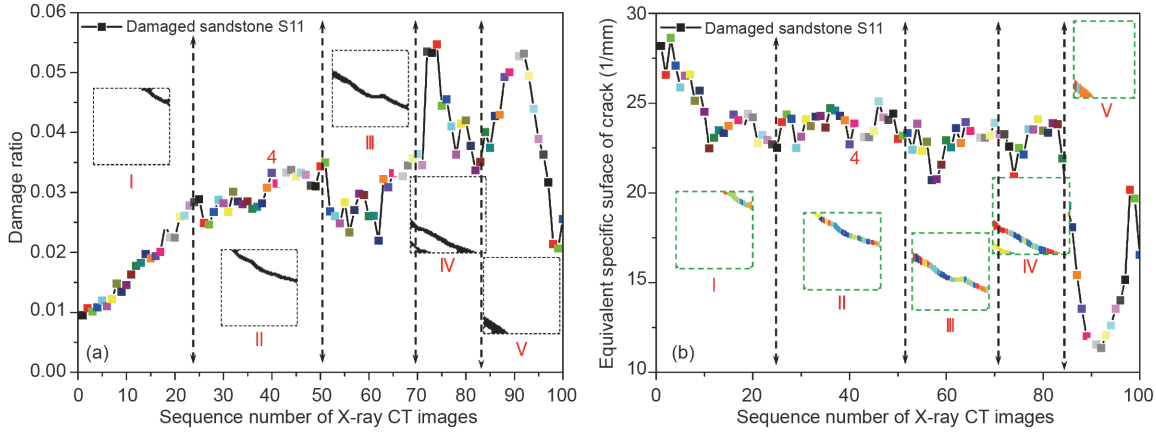

Figure 8 Fracture evolution process of sandstone S11 for (a) damage ratio with crack images at each stage and (b) specific surface of crack with crack images at each stage.

surface almost keeps constant, as shown in the phase II. In the phase III, the crack propagates unstably, and the specific surface fluctuates due to the unstable propagation of crack. In the phase IV, the secondary crack propagation leads to the obvious fluctuation of specific surface. In the phase V, the crack propagates to the edge of the sample, and the specific surface fluctuates sharply.

3.2 Pore scale variables

To improve the accuracy of the correlations derived from pore scale variables, and to predict hydraulic properties, pore scale variables should be precisely estimated from the variety of pore structures (Figure 6) using the proposed method. In addition, 10 types of sandstones containing fine, medium and coarse pores are applied to extract the pore scale variables from their X-ray CT images. The pore scale values can be calculated by eqs. (9)–(22), and the permeability can be estimated by eq. (23).

In total, pore scale variables are all extracted from X-ray CT images of sandstone samples. Figure 9 shows the porosity and specific surface of undamaged sandstone samples S3 and S11 and damaged sandstone sample S11. Obviously, these curves show good opposite correlations between the porosity and specific surface, as described in eq. (14). It should be a reliable evidence for the accuracy and reliability of this correlation between porosity and specific surface.

Figure 10 shows the relative content distribution of specific surface and porosity extracted from 11 types of sandstone samples (Figure 6). Fine pore sandstone samples S2, S4, S5 and S11 have the highest peak in their distribution curves, and coarse pore sandstone samples S6, S7, S8 and S10 have the lowest peak in their distribution curves. In total, the specific surface varies from 34.58 to 77.64 (1/mm) with an average of 54.19 (1/mm). The porosity changes from 0.142 to 0.345 with an average of 0.213. More details are shown in Table 2.

Figure 11 schematically illustrates the relative content distribution of equivalent pore and grain size for these 11 types of sandstone samples. The average gain size denoted by its spherical radius varies from 64.40 to 161.74 μm, and its corresponding standard error varies from 31.42 to 76.10 μm. The average pore radius changes from 29.25 to 53.64 μm, and its corresponding standard error varies from 12.16 to 36.22 μm. The detailed datasets are listed in Table 3. Generally, fine pore sandstone samples show the highest peak and the narrowest distribution, followed by medium and coarse pore sandstone samples in turn.

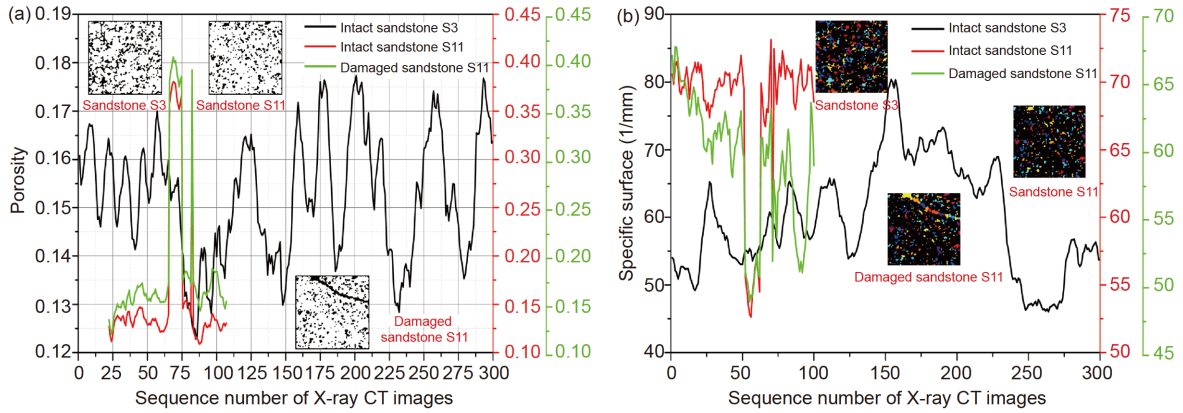

Figure 9 Porosity (a) and specific surface (b) distribution curves with schematic pore-crack images of sandstone S3 and sandstone S11.

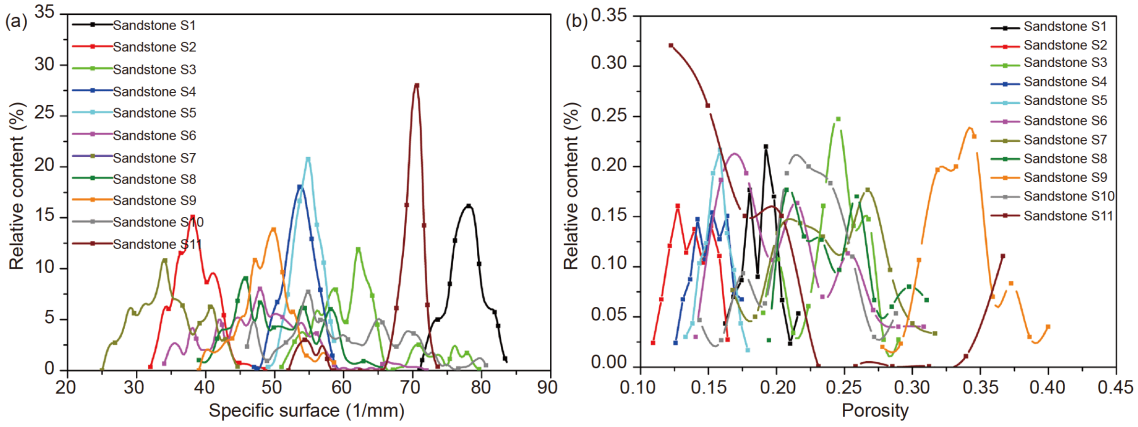

Figure 10 Relative content of specific surface and porosity for different types of sandstone samples.

Table 2 Results analysis of the 11 types of sandstone samples[a)]

Rock types	S1	S2	S3	S4	S5	S6	S7	S8	S9	S10	S11
Sample numbers	26	25	28	12	9	14	29	15	15	14	14
φ	0.191	0.142	0.241	0.153	0.162	0.212	0.244	0.253	0.345	0.227	0.168
ξ_M (1/mm)	83.96	43.94	54.74	53.38	60.03	53.32	31.04	65.69	52.05	63.55	70.86
ξ_C (1/mm)	80.23	40.92	54.29	50.42	56.73	50.62	27.44	61.84	49.63	60.41	68.70
γ	5.95	7.20	5.89	7.33	7.12	5.71	5.83	5.66	5.69	5.72	7.35

a) ξ_M and ξ_C are respectively the experimental and estimated specific surface.

3.3 Permeability

To validate the reliability and accuracy of the proposed approach in Sect. 2, the specific surface and porosity are calculated by eqs. (11)–(22). The comprehensive factor represented by porosity and grain size is first calculated by the measured data extracted from 11 types of fine, medium and coarse pores sandstone samples. Considering that the difference of pore structures leads to the difference of porosity, grain size and specific surface, an average comprehensive correlation factor is applied to calculate the specific surface of sandstone samples. Thus, the specific surface in this study can be written as

$$\xi = 6.27 \times \frac{1-\varphi}{\bar{\lambda}}. \tag{24}$$

Consequently, the real specific surface can be estimated by eq. (24). Figure 12(a) shows the comprehensive correlation factors obtained from fine, medium and coarse pores sandstone samples. Figure 12(b) illustrates the relation between the estimated specific surface and the equivalent radius under different porosity, which is a lookup table of specific surface with known porosity and grain size.

Figure 13 shows the relative content distribution of porosity and specific surface of intact and damaged sandstone

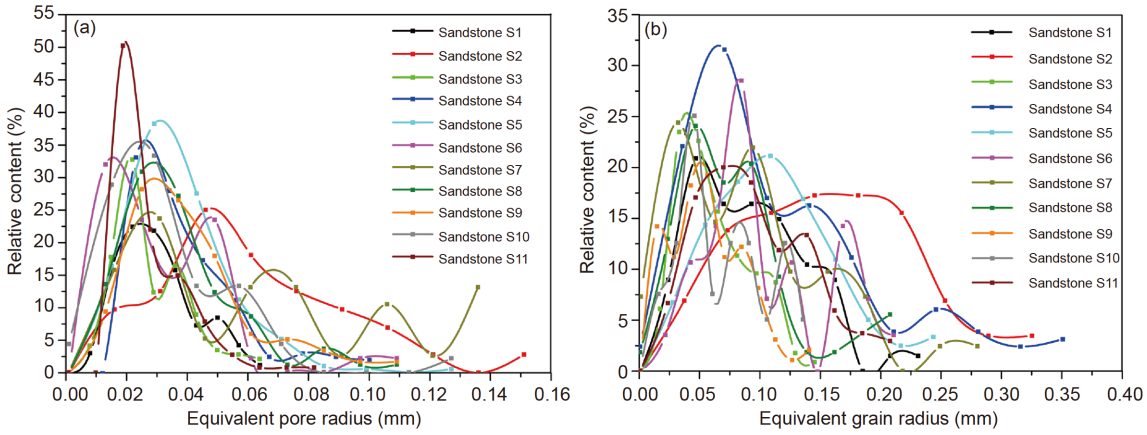

Figure 11 Relative content distributions of equivalent pore and grain size for different types of sandstone samples.

Table 3 Pore and grain sizes of 11 types of sandstone samples

Rock types	Average pore size (μm)			Standard errors (μm)		
	Maxima	Minima	Average	Maxima	Minima	Average
S1	34.41	27.82	30.16	17.46	12.87	14.90
S2	63.67	43.99	53.64	37.72	19.60	28.47
S3	42.94	26.78	35.29	24.92	11.86	17.19
S4	46.49	35.06	39.35	21.01	14.55	17.49
S5	41.38	35.35	37.84	20.64	13.55	16.64
S6	55.67	29.71	40.54	38.22	16.41	25.26
S7	66.31	42.98	52.51	57.99	23.11	36.22
S8	49.71	32.94	40.77	34.16	15.93	22.69
S9	51.10	35.68	41.98	30.11	17.23	21.78
S10	38.38	24.96	31.89	28.15	12.05	20.07
S11	38.22	26.80	29.25	18.17	10.50	12.16
Rock types	Average grain size (μm)			Standard errors (μm)		
	Maxima	Minima	Average	Maxima	Minima	Average
S1	99.46	72.62	82.93	55.05	28.86	41.26
S2	185.34	142.63	161.37	104.53	57.81	76.1
S3	82.85	60.25	72.21	41.73	25.40	31.42
S4	133.25	98.77	116.37	72.30	47.83	59.16
S5	122.84	99.96	109.47	63.15	39.88	51.12
S6	117.84	69.87	92.49	65.62	38.56	50.91
S7	150.82	77.69	106.13	106.19	51.1	77.02
S8	89.57	68.30	78.13	60.80	36.80	48.28
S9	71.42	55.09	63.40	43.83	28.03	34.08
S10	86.62	59.37	70.57	47.67	26.13	35.91
S11	107.96	53.35	90.53	57.65	23.9	43.67

samples S11. Obviously, the distributions of these two samples are similar to each other. However, due to the crack propagation, the increase of void spaces leads to local change of porosity and specific surface. In addition, the damage ratio and specific surface distribution of cracks is similar to that of the void space. Thus, it is concluded from eq. (23) that the permeability increases due to the crack propagation.

Exactly, once the specific surface and porosity of geomaterials are determined, the permeability can be obtained. To validate the reliability and accuracy of the proposed correlations, the estimated specific surface and permeability are compared with the measured specific surface and perme-

ability for the 11 types of sandstone samples. Figure 14(a) shows the correlation between the estimated and measured specific surface. The correlation coefficient reaches to 0.98, which implies the precision of the proposed correlations. Figure 14(b) shows the histogram of estimated and measured permeability. The estimated permeability (black) well agrees with the laboratory measured permeability (red). The average permeability values are respectively 245, 512 and 561 mD

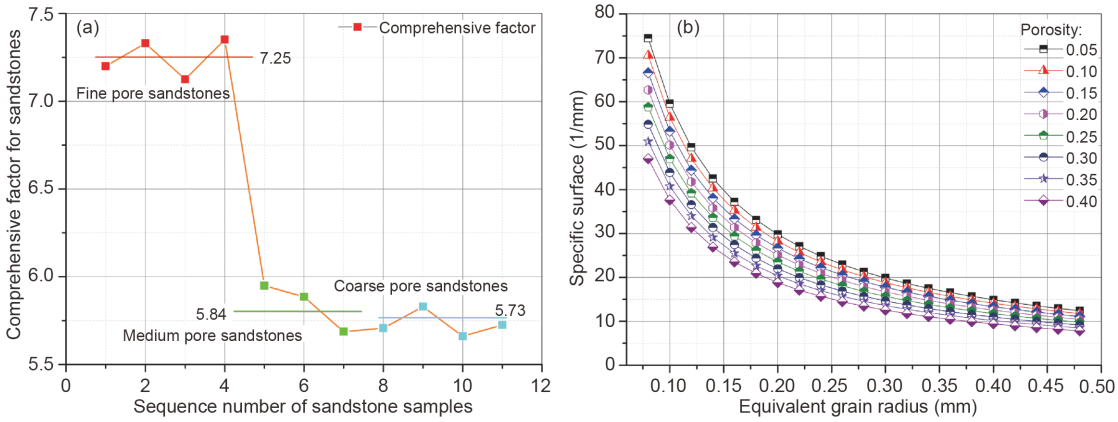

Figure 12 Estimated results of sandstone samples for (a) comprehensive factor and (b) specific surface versus grain size under different porosity.

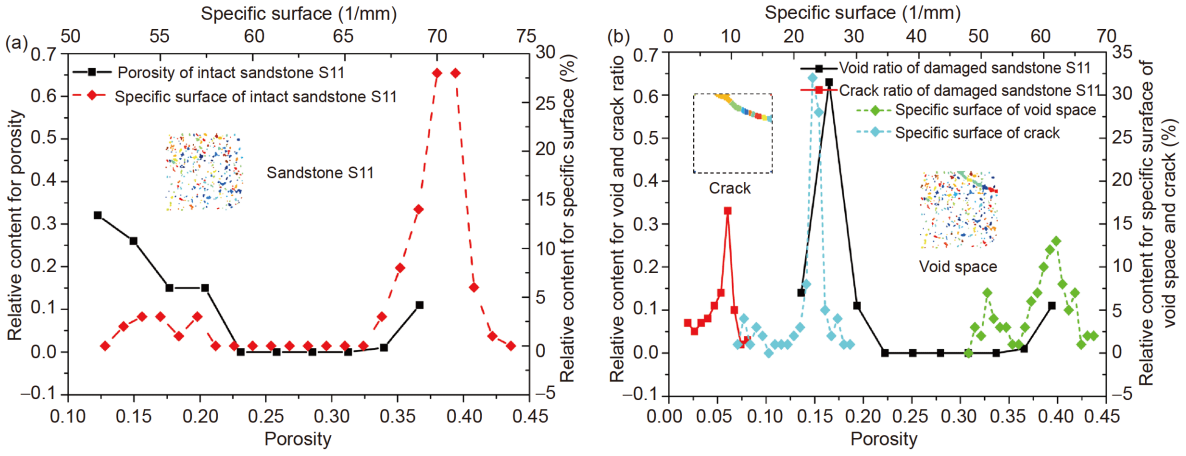

Figure 13 Relative content of porosity and specific surface from sandstone S11 for (a) intact samples and (b) damaged samples.

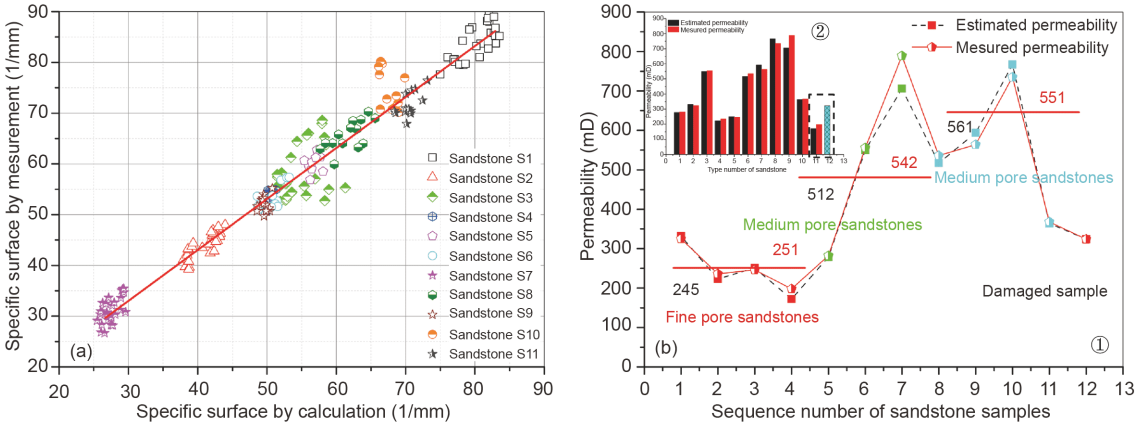

Figure 14 Comparison of the laboratory measured value and estimated value for (a) specific surface (R^2=0.98432) and (b) permeability for sandstone samples S1–S11.

for estimated results and 251, 542 and 551 mD for the laboratory measured permeability, which increases from fine pore sandstones to coarse pore sandstone samples. Moreover, the permeability obtained from the intact sandstone sample S11 (172 and 198 mD for estimated and laboratory measured result, respectively) is lower than that obtained from the damaged sandstone sample S11 (blue, 324 mD), which implies that fracture improves the permeability in the damaged sandstone samples.

4 Summary and conclusions

In this study, a double threshold segmentation algorithm is proposed to segment the pore structures of X-ray CT images for different types of sandstone samples. The pore scale variables are extracted from the segmented images. A novel correlation for permeability derived from pore scale variables is proposed and validated by the proposed 3D MPNP model. The fracture characteristics and permeability are investigated as well. The main conclusions are drawn as follows.

(1) The proposed double threshold algorithm is not only applicable to distinguish the pores and cracks of sandstone, but also useful for other porous geomaterials. Thus, the pore scale variables can be estimated, and the hydraulic, fracturing behaviors can be studied.

(2) Pore scale variables can be extracted from the segmented pores-crack-gains image. The distribution characteristics of the pore scale variables are useful to investigate the hydraulic and fracture characteristics.

(3) The permeability of different types of geomaterials can be simply predicted by the proposed relations among these pore scale variables. Therefore, it becomes easier and more efficient to obtain the hydraulic properties compared with the classical permeability prediction methods.

(4) The proposed equations are not only applicable for sandstone, but also can be employed to estimate the pore scale variables of other porous geomaterials. By considering suitable numbers of samples, the precision can be improved for comprehensive factor, which increases the availability of these correlations.

This work was supported by the National Natural Science Foundation of China (Grant Nos. 51839009 and 51679017), and the Graduate Research and Innovation Foundation of Chongqing, China (Grant No. CYB18037).

1 Xiao D, Lu S, Yang J, et al. Classifying multiscale pores and investigating their relationship with porosity and permeability in tight sandstone gas reservoirs. Energy Fuels, 2017, 31: 9188–9200
2 Ojha S P, Misra S, Tinni A, et al. Relative permeability estimates for Wolfcamp and Eagle Ford shale samples from oil, gas and condensate windows using adsorption-desorption measurements. Fuel, 2017, 208: 52–64
3 Zhao Y, Yu Q. CO_2 breakthrough pressure and permeability for unsaturated low-permeability sandstone of the Ordos Basin. J Hydrol, 2017, 550: 331–342
4 Liu Z, Cheng Y, Wang L, et al. Analysis of coal permeability rebound and recovery during methane extraction: Implications for carbon dioxide storage capability assessment. Fuel, 2018, 230: 298–307
5 Ameli A A, Amvrosiadi N, Grabs T, et al. Hillslope permeability architecture controls on subsurface transit time distribution and flow paths. J Hydrol, 2016, 543: 17–30
6 Elger J, Berndt C, Rüpke L, et al. Submarine slope failures due to pipe structure formation. Nat Commun, 2018, 9: 715
7 Zhao Z, Zhou X P. Digital energy grade-based approach for crack path prediction based on 2D X-ray CT images of geomaterials. Fatigue Fract Eng Mater Struct, 2019, 42: 1292–1307
8 Honarpour M, Mahmood S M. Relative-permeability measurements: An overview. J Pet Tech, 1988, 40: 963–966
9 Gomez C T, Dvorkin J, Vanorio T. Laboratory measurements of porosity, permeability, resistivity, and velocity on fontainebleau sandstones. Geophysics, 2010, 75: E191–E204
10 Chen J, Yang X, Duan Q, et al. Integrated measurements of permeability, effective porosity, and specific storage of core samples using water as the pore fluid. Int J Rock Mech Min Sci, 2015, 79: 55–62
11 Qajar J, Arns C H. Characterization of reactive flow-induced evolution of carbonate rocks using digital core analysis-part 1: Assessment of pore-scale mineral dissolution and deposition. J Contam Hydrol, 2016, 192: 60–86
12 Tahmasebi P, Hezarkhani A. A fast and independent architecture of artificial neural network for permeability prediction. J Pet Sci Eng, 2012, 86-87: 118–126
13 Mohamed M T. Performance of fuzzy logic and artificial neural network in prediction of ground and air vibrations. Int J Rock Mech Min Sci, 2011, 48: 845–851
14 Saemi M, Ahmadi M, Varjani A Y. Design of neural networks using genetic algorithm for the permeability estimation of the reservoir. J Pet Sci Eng, 2007, 59: 97–105
15 Okabe H, Blunt M J. Pore space reconstruction using multiple-point statistics. J Pet Sci Eng, 2005, 46: 121–137
16 Al-Kharusi A S, Blunt M J. Network extraction from sandstone and carbonate pore space images. J Pet Sci Eng, 2007, 56: 219–231
17 Ranaee E, Porta G M, Riva M, et al. Prediction of three-phase oil relative permeability through a sigmoid-based model. J Pet Sci Eng, 2015, 126: 190–200
18 Shams M, Raeini A Q, Blunt M J, et al. A numerical model of two-phase flow at the micro-scale using the volume-of-fluid method. J Comput Phys, 2018, 357: 159–182
19 Haeri H, Marji M F, Shahriar K, et al. On the HDD analysis of micro crack initiation, propagation, and coalescence in brittle materials. Arab J Geosci, 2015, 8: 2841–2852
20 Haeri H, Shahriar K, Marji M F, et al. Modeling the propagation mechanism of two random micro cracks in rock samples under uniform tensile loading. In: Proceedings of the 13th International Conference on Fracture. Beijing, 2013
21 Haeri H, Sarfarazi V, Marji M F, et al. Experimental and numerical study of shear fracture in brittle materials with interference of initial double cracks. Acta Mech Solid Sin, 2016, 29: 555–566
22 Sarfarazi V, Haeri H. A review of experimental and numerical investigations about crack propagation. Comput Concrete, 2016, 18: 235–266
23 Behrang A, Mohammadmoradi P, Taheri S, et al. A theoretical study on the permeability of tight media; effects of slippage and condensation. Fuel, 2016, 181: 610–617
24 Becker I, Wüstefeld P, Koehrer B, et al. Porosity and permeability variations in a tight gas sandstone reservoir analogue, westphalian d, lower saxony basin, nw germany: influence of depositional setting and diagenesis. J PetGeol, 2017, 40: 363–389
25 Sun W C, Wong T F. Prediction of permeability and formation factor of sandstone with hybrid lattice Boltzmann/finite element simulation on micro tomographic images. Int J Rock Mech Min Sci, 2018, 106:

269–277
26 Weerakone W B, Wong R C K, Kantzas A. Morphological characterization of induced fracture in sandstone using X-ray computed tomography scanning. Geotech Testing J, 2012, 35: 460–468
27 Alhammadi A M, AlRatrout A, Bijeljic B, et al. Pore-scale imaging and characterization of hydrocarbon reservoir rock wettability at subsurface conditions using X-ray microtomography. J Vis Exp, 2018, 140: e57915
28 Jobmann M, Billaux D. Fractal model for permeability calculation from porosity and pore radius information and application to excavation damaged zones surrounding waste emplacement boreholes in opalinus clay. Int J Rock Mech Min Sci, 2010, 47: 583–589
29 Zheng J, Zheng L, Liu H H, et al. Relationships between permeability, porosity and effective stress for low-permeability sedimentary rock. Int J Rock Mech Min Sci, 2015, 78: 304–318
30 Ingraham M D, Bauer S J, Issen K A, et al. Evolution of permeability and Biot coefficient at high mean stresses in high porosity sandstone. Int J Rock Mech Min Sci, 2017, 96: 1–10
31 Alyafei N, Blunt M J. Estimation of relative permeability and capillary pressure from mass imbibition experiments. Adv Water Resources, 2018, 115: 88–94
32 Sufian A, Russell A R. Microstructural pore changes and energy dissipation in Gosford sandstone during pre-failure loading using X-ray CT. Int J Rock Mech Min Sci, 2013, 57: 119–131
33 Oliveira T D S, Blunt M J, Bijeljic B. Modelling of multispecies reactive transport on pore-space images. Adv Water Resources, 2019, 127: 192–208
34 Latief F D E, Fauzi U, Bijaksana S, et al. Pore structure characterization of 3D random pigeon hole rock models. Int J Rock Mech Min Sci, 2010, 47: 523–531
35 Du S, Li M J, Ren Q, et al. Pore-scale numerical simulation of fully coupled heat transfer process in porous volumetric solar receiver. Energy, 2017, 140: 1267–1275
36 Sun W C, Wong T F. Prediction of permeability and formation factor of sandstone with hybrid lattice Boltzmann/finite element simulation on micro tomographic images. Int J Rock Mech Min Sci, 2018, 106: 269–277
37 Zhao Z, Zhou X P. An integrated method for 3D reconstruction model of porous geomaterials through 2D CT images. Comput Geosci, 2019, 123: 83–94
38 Yang L, Ai L, Xue K, et al. Analyzing the effects of inhomogeneity on the permeability of porous media containing methane hydrates through pore network models combined with CT observation. Energy, 2018, 163: 27–37
39 Dong H, Blunt M J. Pore-network extraction from micro-computerized-tomography images. Phys Rev E, 2009, 80: 036307
40 Kachanov L M. Rupture time under creep conditions. Int J Fracture, 1999, 97: 11–18
41 Rabotnov Y N. Paper 68: On the equation of state of creep. In: Proceedings of the Institution of Mechanical Engineers, Conference Proceedings. London: SAGE Publications, 1963
42 Murakami S. Continuum damage mechanics: A continuum mechanics approach to the analysis of damage and fracture. Springer Ebooks, 2012. 4731–4755
43 Pape H, Tillich J E, Holz M. Pore geometry of sandstone derived from pulsed field gradient NMR. J Appl Geophys, 2006, 58: 232–252
44 Jeong N. Advanced study about the permeability for micro-porous structures using the lattice boltzmann method. Transp Porous Media, 2010, 83: 271–288
45 Xie C, Raeini A Q, Wang Y, et al. An improved pore-network model including viscous coupling effects using direct simulation by the lattice Boltzmann method. Adv Water Resources, 2017, 100: 26–34
46 Henderson N, Brêttas J C, Sacco W F. A three-parameter Kozeny-Carman generalized equation for fractal porous media. Chem Eng Sci, 2010, 65: 4432–4442
47 Xu P, Yu B. Developing a new form of permeability and Kozeny-Carman constant for homogeneous porous media by means of fractal geometry. Adv Water Resources, 2008, 31: 74–81
48 Li B, Wong R C K, Heidari S. A modified Kozeny-Carman model for estimating anisotropic permeability of soft mudrocks. Mar PetGeol, 2018, 98: 356–368
49 Mohammadmoradi P, Kantzas A. Pore-scale permeability calculation using CFD and DSMC techniques. J Pet Sci Eng, 2016, 146: 515–525
50 Peyman M, Apostolos K. Modelling two-phase flow in multi-mineral porous media using coupled level set-volume of fluid (CLSVOF) method. In: Proceedings of the GeoConvention 2016: Optimizing Resources. Calgary, 2016
51 Kozeny J. Ueber kapillare leitung des wassers im boden. Sitzungsber Akad Wiss Wien, 1927, 136: 271–306
52 Carman P C. Fluid flow through granular beds. Trans Inst Chem Eng, 1937, 15: 150–66
53 McCabe W L. Unit Operations of Chemical Engineering. 7th ed. New York: McGraw-Hill, 2005
54 Tiab D, Donaldson E C. Petrophysics: Theory and Practice of Measuring Reservoir Rock and Fluid Transport Properties. Houston: Gulf Professional Publishing, 2011